Article

Unraveling the Molecular Structure of Zeolite−Octyl Methoxycinnamate Hybrid UV Filters: A Combined Spectroscopic and Computational Approach

Michael Fischer, Riccardo Fantini, Rossella Arletti, Jakob Brauer, and Lorenzo Mino*

Read Online

ACCESS | 📊 Metrics & More | 📄 Article Recommendations | 🅢🅘 Supporting Information

ABSTRACT: In this contribution, we tried to shed light on the molecular structure of octyl methoxycinnamate (octinoxate, OMC) adsorbed in NaX zeolite, which represents a promising hybrid UV filter system. The combination of infrared spectroscopy and density functional theory modeling was crucial to identify all the complex host−guest interactions and to unveil that, although slightly thermodynamically unfavored, OMC is dominantly present in the *trans*-form inside the NaX framework. We also showed that the interaction between the zeolite Na cations and the OMC molecule is the key feature that determines the stability and efficacy of these hybrid UV filters. These findings confirm that cationic zeolites are promising materials for the encapsulation of UV filters to decrease their negative impact on the environment and their photochemical instability.
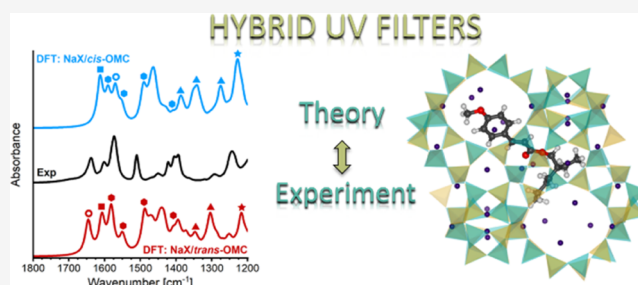
1. INTRODUCTION

Sunlight is the main external energy source for Earth; the solar spectrum is constituted by infrared rays (IR, wavelength range 750 nm −1 mm), visible light (Vis, 400−750 nm), and ultraviolet rays (UVR or UV, 100−400 nm). About 8.3% of the solar radiation at the Earth's surface is represented by UVR, while visible and infrared radiations represent 42.3 and 49.4%, respectively.[1] UV rays are further divided into UVA (315−400 nm), UVB (280−315 nm), and UVC (100−280 nm), which account for about 6.3, 1.5, and 0.5%, respectively.

Despite its quite low contribution to sunlight, UV radiation has an important impact on human health; indeed, balanced sunlight exposure is of paramount importance in preventing health issues. On the one hand, correct and safe UVR exposure is responsible for the production of about 90% of the requirement for vitamin D in humans,[2] and health issues arise from UVB exposure deficit.[3] On the other hand, UVR is linked to most of the adverse effects of excessive and unprotected solar exposure and is considered the main cause of skin carcinogenesis and sensitization.[4,5]

During the last decades, the number of skin cancers diagnosed annually increased continuously, including both malignant melanoma (MM) and nonmelanoma skin cancer (NMSC).[6] The American Cancer Society estimates 106,110 new cases of MM in the United States for 2021, with over 7,000 deaths.[7] Also, European countries reported an overall increase in melanoma incidence rate.[8] Skin cancer is also a cost burden for many countries.[9]

Fortunately, the public has become more and more conscious of the adverse effects of excessive exposure to UVR. Thus, the paramount importance of skin cancer has elicited strong research interest for the development of more effective and safe UV filters (UVfs). UVFs have become almost ubiquitous in personal-care products such as sunscreens, shampoo, shower gels, and body lotions.[10]

Sunscreen formulations are, in fact, the main method of health protection against solar exposure. The main targets of an ideal sunscreen are protection against sunburns, skin aging, skin sensitization, and skin carcinogenesis. Sunscreen must provide broad-spectrum UV protection, filtering both UVB and UVA, and possibly also the shortest visible light beyond 400 nm.

Sunscreen formulations are complex mixtures of different compounds, basically UV filters, emollients, and emulsifiers. UVfs are the real active component of sunscreens absorbing UV rays; for effective UV protection, UVfs should form a uniform layer on the skin and remain stable and active during the whole UV exposure. In order to prevent undesired allergic reactions, UVfs should not permeate the viable skin.[11]
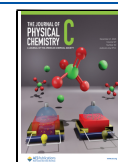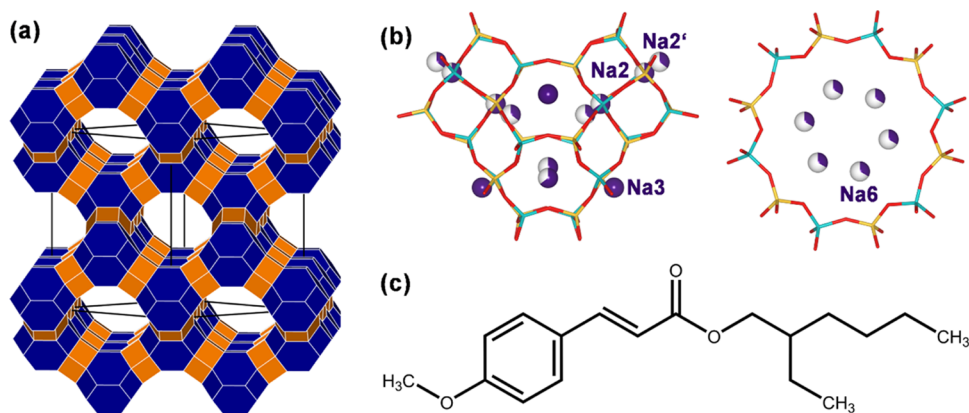
Figure 1. (a) FAU framework topology. Sodalite (*sod*) cages and double six-membered rings (*d6r*) are shown as solid blue and orange building blocks, respectively; the FAU "supercages" connected by 12MRs are transparent. (b) Na sites associated with *sod* and *d6r* cages (Na2/Na2′/Na3) and with 12MR rings (Na6). Yellow = Si, cyan = Al, red = O, and purple = Na; fractionally occupied sites are represented by partially colored spheres. (c) Molecular structure of OMC.

UVfs are organic or inorganic compounds that absorb UV photons reaching excited electronic states and then dissipating energy without losing efficacy. Most UVfs have limited absorption ranges, and for these reasons, several filters are combined to obtain broad-spectrum protection.

Many issues linked to the use of UV filters remain: first of all, their photochemical instability, in fact, exposure to UV radiation, can lead to photochemical reactions that compromise their safety and efficacy;[12,13] also, not less important, their impact on the environment.

Due to their high lipophilicity and low biodegradability,[14] UV filters, especially the organic ones, can bioaccumulate at different trophic levels,[15] particularly in fatty tissues, in all the exposed organisms (e.g., mussels, crustaceans, eels, fish, marine mammals, and aquatic birds, see e.g., refs 16−18).

Recently, a method to improve the stability of UV filters in sunscreen formulation involving the molecules encapsulation in a zeolitic matrix has been proposed by our group.[19] Zeolites are microporous materials showing different systems of channels and cages[20] that have been used for the encapsulation of several organic molecules[21−25] and, very recently, for the encapsulation and shielding of UVfs.[19] Our recent research showed that the encapsulation of avobenzone (butylmethoxy dibenzoylmethane, $C_{20}H_{22}O_3$, AVO) and octinoxate (octyl methoxycinnamate, $C_{18}H_{26}O_3$, OMC), which are two of the most used organic UVfs, in cationic zeolites (i.e., zeolite L and NaX-FAU) is highly efficient, resulting in an enhanced UV filtering capacity. Selected systems among those studied have been characterized by experimental crystallographic techniques in order to gain knowledge regarding the mechanism of stabilization and the phenomena occurring in the material. In fact, understanding the effects of spatial confinement on filter stability is of paramount importance for the further development of this interesting new class of materials. In a recently published paper,[26] thanks to the combination of X-ray powder diffraction and spectroscopic techniques, it has been possible to define the position of OMC molecules in the channels of zeolite L (LTL/OMC) and to elucidate the host−guest and guest−guest interactions arising from the encapsulation. It was demonstrated that the OMC molecules were located in the 12-membered ring (12MR) main channel, establishing links between the carbonyl group oxygen and zeolite extraframework K cations. This interaction probably dominates the

stability and efficacy of LTL/OMC material and may explain why—among different systems studied and reported by our group elsewhere[19]—the cationic zeolites display the most promising features for possible future applications for the encapsulation of UV filters.

The aim of this paper is to investigate the interaction of the same molecule (OMC) with another zeolite, that is NaX (framework type FAU[20]). This hybrid material, along with LTL/OMC, previously investigated from the structural point of view,[26] is a promising candidate since it shows high stability and efficacy and would be of paramount importance to compare the two systems to draw a complete picture of the interaction driving the stability and the efficacy of these filters. Unfortunately, the high symmetry of X zeolite, coupled with the complexity of the guest molecule, prevents a structural refinement of diffraction data, and for this reason, we propose a multi-technique approach, involving both infrared spectroscopic experiments under controlled atmosphere and electronic structure calculations in the framework of dispersion-corrected density functional theory (DFT) to unravel the structure of a stable zeolite-UV filter hybrid, that is NaX/OMC.

2. MATERIALS AND METHODS

2.1. Materials. Octinoxate ($C_{18}H_{26}O_3$, liquid, molar weight (MW) 290.40 g/mol, specific gravity (SG) 1.01 g/mL, purity >96,0%) was purchased from TCI (Tokyo Chemical Industry Co., Ltd.). Faujasite zeolite (framework type FAU,[20] Figure 1) was used in its sodic low-silica forms (13X-FAU, Si/Al = 1.2) and was purchased from BDH Chemicals (Product 54017, out of stock). The FAU structure is characterized by a tridimensional 12MR channel system (maximum diameter of a sphere that can diffuse along them: 7.35 Å). NaX-FAU has Na cations spread over different crystallographic sites, accounting for about 90 Na per unit cell (p.u.c.), and it will be labeled as NaX in the following.

2.1.1. Hybrid NaX/OMC Preparation. The NaX zeolite was dehydrated at 450 °C for 3 h before UVF loading to remove all the H_2O molecules and mixed, at room temperature, with neat OMC in a glass tube. The mixture was stirred, homogenized, sealed, and heated at 100 °C for 48 h. The sample was then washed with acetone to remove the unloaded UV filter present on the external surface of the zeolite grains. Before analysis, the

sample was dried for 48 h at 60 °C for solvent removal after the washing process. Details of sample preparation are available in ref 19.

2.2. Methods. *2.2.1. FT-IR Spectroscopy.* To perform FT-IR measurements, the NaX/OMC sample was pressed in self-supporting pellets ("optical density" of ca. 10 mg·cm^{-2}) and placed in quartz cells equipped with KBr windows, enabling *in situ* data acquisition during adsorption−desorption experiments.[27] For the outgassing procedure and the thermal treatments, the cells were connected to a conventional vacuum line (residual pressure <1 × 10^{-4} mbar). The IR spectra were acquired using a Bruker Equinox 55 spectrometer equipped with an MCT detector. For each spectrum, 128 interferograms at 2 cm^{-1} were averaged. The IR spectrum of the isolated octinoxate molecule was acquired in a transmission cell for liquids by diluting 15 μL of $C_{18}H_{26}O_3$ in 785 μL of CCl_4.

2.2.2. Computational Models and Force Field Calculations. For the computational modeling, a fully ordered structure model of NaX was used based on the experimental crystal structure data of the dehydrated form at room temperature (space group $Fd\bar{3}$, a = 24.98 Å).[28] First of all, a fully ordered distribution of Si and Al with a Si/Al ratio of 1.0 was assumed, resulting in a framework composition of [$Al_{96}Si_{96}O_{384}$]. Al atoms were placed at the T2 site of the experimental crystal structure. For charge balance, 96 Na cations were distributed over four experimentally observed sites (Na2/Na2′, Na3, Na6)[28] in a way that experimental occupancies were matched as closely as possible while at the same time avoiding close cation−cation contacts (see the Supporting Information, section S1 for more details). To study the adsorption of OMC, models of the *cis*- and *trans*-forms of OMC were taken from a previous computational study by Fois et al.[29] After optimization of the structures of NaX and *cis*-/*trans*-OMC using DFT (see the following subsection), adsorption configurations of both isomers in the pores of NaX were generated using preliminary force field simulations. Loadings of 1 and 4 OMC p.u.c. were considered in these calculations, which employed the *Adsorption Locator* module of the DS Biovia "Materials Studio" suite. This module allows the determination of low-energy adsorption configurations from Monte Carlo simulations with slowly decreasing temperature (simulated annealing, temperature range 10,000 K → 100 K). The COMPASS III force field was used in these simulations,[30] in which all zeolite atoms, including Na cations, were fixed at their initial positions. Typically, 30 separate annealing cycles were run for each isomer and loading. Among the resulting 30 configurations, 5 distinct low-energy configurations were selected for the following DFT calculations.

2.2.3. DFT Calculations. All DFT calculations were performed with the Quickstep code within the CP2K package (version 9.1), which uses the Gaussian and plane-wave (GPW) method.[31,32] To account for dispersion interactions, the rev-vdW-DF2 functional was employed.[33] The calculations used "molecularly optimized" basis sets distributed with the CP2K code (BASIS_MOLOPT)[34] and Goedeker−Teter−Hutter pseudopotentials devised by Krack.[35] The first Brillouin zone was sampled at the Γ point only. Structure optimizations were carried out with double-ζ basis sets using a plane-wave cutoff energy of 600 Ry. To compute adsorption energies, single-point calculations were subsequently run for the optimized structures, using triple-ζ basis sets and a cutoff energy of 900 Ry, in keeping with earlier work.[36] For a given complex, the adsorption energy was calculated as

$$E_{ads} = (E_{DFT}[NaX/\textit{cis- or trans-}OMC] - E_{DFT}[NaX] - N \cdot E_{DFT}[\textit{trans-}OMC])/N$$

where N = 1 or 4. The first term on the right-hand side corresponds to the DFT energy of the adsorption complex of *cis*- or *trans*-OMC in NaX, the second term is the DFT energy of the zeolite without OMC, and the third term is the DFT energy of *trans*-OMC in the gas phase. For isolated OMC (*cis* and *trans*) and selected NaX/OMC adsorption configurations, the IR spectra were predicted with DFT calculations employing the finite displacement method. For computational efficiency, only displacements of the guest molecules were considered for the NaX/OMC systems. Additional calculations, including cation displacements, revealed no prominent impact in the wavenumber range of most interest (1800−1200 cm^{-1}). DFT-calculated IR spectra were plotted using MOLDEN,[37] employing a Lorentzian broadening with a full width at half-maximum of 10 cm^{-1}.

For the nonlocal rev-vdW-DF2 exchange−correlation functional, there is no simple way to separate the contribution of dispersion interactions from the total adsorption energy. In order to estimate the magnitude of dispersion interactions, the DFT energies were recomputed using the PBE-D3 functional[38,39] for structures previously optimized with the rev-vdW-DF2 functional. For PBE-D3, the pairwise dispersion correction term can easily be separated from the total energy. Table S1 lists the PBE-D3 energies and the dispersion-only contribution as well as various other intermediate values of adsorption energies. Although PBE-D3 delivers systematically more negative adsorption energies than rev-vdW-DF2, it is worth noting that the correlation is excellent (Figure S2), providing confidence that the PBE-D3 results should at least provide a semiquantitative estimate of the relative importance of dispersion interactions.

3. RESULTS AND DISCUSSION

3.1. FT-IR Study of NaX/OMC. As the first step of our spectroscopic study, we studied the IR spectrum of the NaX/OMC sample in air (Figure 2, light blue curve), which is dominated in the 1800−1200 cm^{-1} range by the vibrational modes of the OMC molecules. In particular, we can identify the peaks due to aromatic ring vibrations in the OMC at 1605,
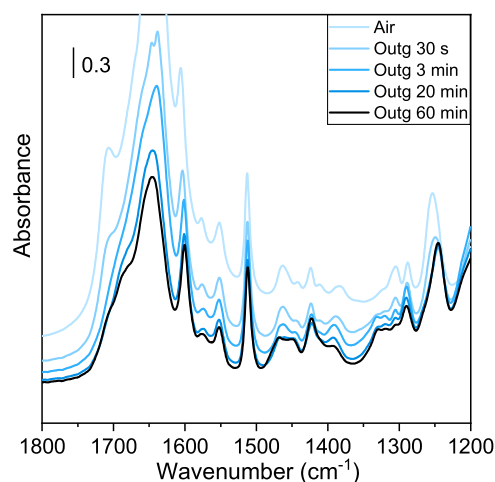

Figure 2. FT-IR spectra of the NaX/OMC sample at increasing outgassing time at room temperature.

1512, and 1423 cm^{-1} (see the computational part below for a more complete assignment of the different vibrational modes). The high wavenumber spectral region, between 3800 and 3000 cm^{-1}, is out of scale owing to the strong absorption of the ν(O–H) stretching mode associated with hydrogen-bonded OMC and water molecules.[40,41] On increasing the outgassing time at room temperature (Figure 2), we can see a progressive decrease of the OMC bands, which indicates the presence of a fraction of loosely bound molecules. In this respect, it is worth discussing the behavior of the ν(C=O) vibration, which shows different components in the 1710−1640 cm^{-1} range. In particular, the shoulder at 1710 cm^{-1} has a frequency very similar to the ν(C=O) signal in the free OMC molecule (*vide infra*), suggesting its assignment to free carbonyl groups interacting with the external zeolite surfaces. This hypothesis is further confirmed by the complete disappearance of this signal upon outgassing the sample at room temperature.

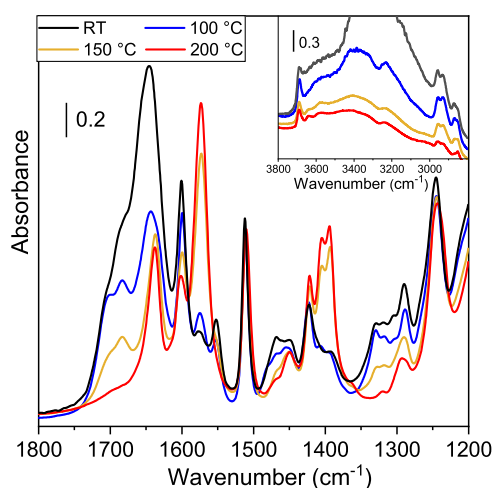Figure 3 shows the effect of outgassing the sample at increasing temperatures up to 200 °C, since at higher

Figure 3. FT-IR spectra of the NaX/OMC sample outgassed for 1 h at increasing temperatures.

temperatures, the OMC filter starts to decompose. The signals related to adsorbed H$_2$O molecules progressively decrease, and the 3800−3000 cm^{-1} range is now in scale (inset of Figure 3). We can, thus, recognize two bands at 3690 and 3648 cm^{-1} ascribed to the stretching mode of hydroxyl groups located in different positions in the zeolite framework.[42−44] In the spectral region of the ν(C=O) vibrations, we can now clearly identify at least three components at 1700, 1683, and 1637 cm^{-1} ascribed to the OMC molecules in which the carbonyl group is involved in increasingly stronger interactions with the NaX framework. This interpretation is also in agreement with the observation that the first two components disappear after outgassing at 200 °C. Moreover, other vibrational modes of the

filter also experience a bathochromic shift upon removal of the adsorbed water and of the less tightly bound OMC molecules. In particular, the stretching mode of the C=C double bond close to the carbonyl shifts from 1640 to 1600 cm^{-1}, and the highest aromatic ring vibration shifts from 1605 to 1573 cm^{-1}.

From the analysis of the IR spectra, a complex picture emerges in which OMC molecules in different local environments are present inside the zeolite, characterized by different stabilities and vibrational properties; thus, a detailed computational study appears to be crucial to elucidate at the molecular level all the possible interactions between the filter and the NaX framework.

3.2. DFT Modeling of OMC Adsorption in the NaX Zeolite. An initial comparison of the DFT total energies of *trans*- and *cis*-OMC showed that the rev-vdW-DF2 functional predicts *trans*-OMC to be favored over the *cis* form by about 19 kJ mol^{-1}. This result is in line with a previous computational study, where similar energy differences were reported for a variety of dispersion-corrected DFT approaches.[29] Therefore, the total energy of *trans*-OMC was used as the reference value in all adsorption energy calculations. Table 1 reports the DFT adsorption energies obtained for the different NaX/OMC adsorption configurations, ordered according to the adsorption energy. As a Boltzmann averaging over all five configurations always delivers energy values that are very close to the E_{ads} value of the lowest-energy case, the most emphasis in the discussion will be placed on the lowest-energy configuration. Additionally, the relative contribution of dispersion interactions (obtained from PBE-D3 calculations, see above) is also given.

At a loading of 1 p.u.c., the calculations indicate an increased stabilization of *cis*-OMC in the pores of NaX in comparison to *trans*-OMC. However, the overall difference in adsorption energy among the lowest-energy configurations is not very large, amounting to about 11 kJ mol^{-1}, or 3% in relative terms. The relative contribution of dispersion interactions typically amounts to about 50% of the total adsorption energy. While this is clearly a significant contribution, it also indicates that other, more localized interactions play an important role in stabilizing the adsorbed OMC molecules. To analyze this in more depth, the lowest-energy configurations of *trans*- and *cis*-OMC are shown in Figure 4. Both notable differences and common features are visible: first, the *trans*-OMC molecule spans two FAU supercages. The methoxyphenyl and octyl moieties occupy different cages, and the central ester group is located approximately at the center of the connecting 12MR window. In contrast, the bulkier, more compact *cis* isomer occupies a single cage. In both cases, there are short contacts between OMC oxygen atoms and Na cations that are located in the 12MR windows (Na6 cations according to the nomenclature used in prior work[28]). The interatomic distances between Na cations and the carbonyl and methoxy oxygen atoms are similar for both isomers, in the range of 2.27 to 2.38

Table 1. DFT Adsorption Energies Obtained for NaX/OMC Adsorption Configurations (rev-vdW-DF2 Results) and Relative Contribution of Dispersion Interactions (PBE-D3 Results)

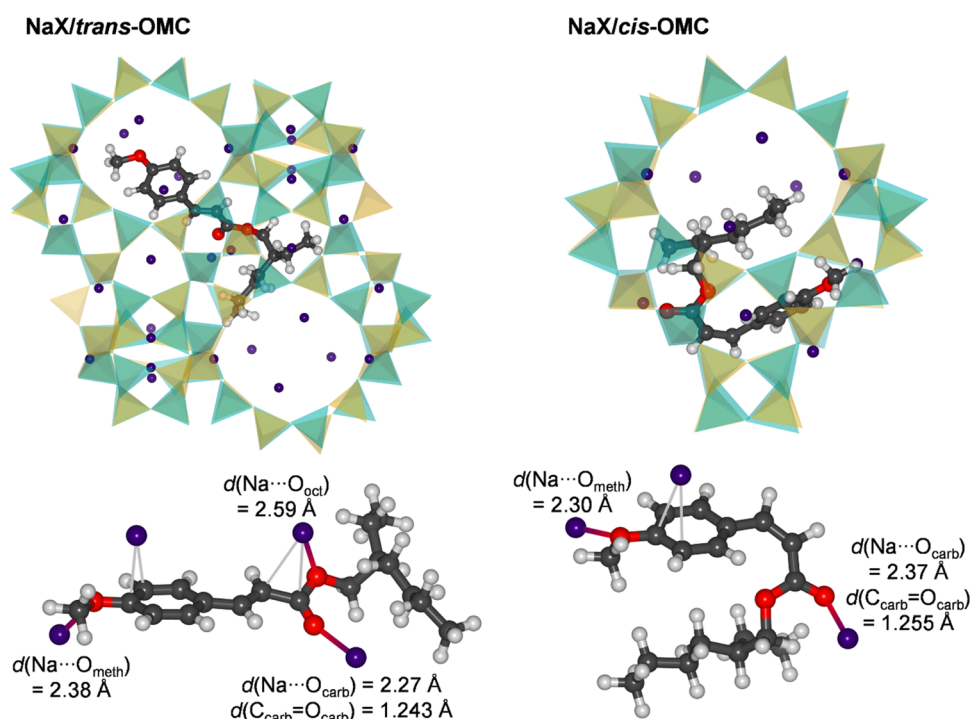| loading	isomer	E_{ads} [kJ mol^{-1}]	E_{disp}/E_{ads} [%]
1 OMC p.u.c.	*trans*	**−380**/−357/−349/−343/−306	47/49/54/50/53
1 OMC p.u.c.	*cis*	**−391**/−388/−384/−377/−364	47/48/46/47/48
4 OMC p.u.c.	*trans*	**−351**/−337/−336/−334/−328	53/56/51/53/56
4 OMC p.u.c.	*cis*	**−361**/−360/−357/−344/−339	51/50/52/53/56

Figure 4. Lowest-energy adsorption configurations of *trans*- and *cis*-OMC in adsorbed NaX at a loading of 1 OMC molecule p.u.c. The complete environment of the adsorbed molecules is visualized in the top panels, whereas the bottom panels show only the OMC molecule and the closest Na cations. Short Na$\cdots$O$_{OMC}$ contacts are represented by gradient lines, with distances given as insets, and Na$\cdots$C$_{OMC}$ distances below 3 Å are indicated by thin gray lines.

Å. The Na$\cdots$O$_{carb}$ interaction results in an elongation of the C$_{carb}$=O$_{carb}$ double bond, which is more prominent for *cis*-OMC (the DFT-optimized bond distances in the free molecule amount to 1.228/1.226 Å for *trans*-/*cis*-OMC). In addition to these short Na$\cdots$O contacts, which are likely dominated by electrostatic interactions, there are also some fairly short distances below 3 Å from Na cations to some C atoms of the phenyl ring and (for NaX/*trans*-OMC) of the C=C double bond. These contacts point to a certain role of cation$-\pi$ interactions.[45,46]

At an increased loading of 4 OMC p.u.c., which is fairly close to the experimental loading for the as-synthesized samples (i.e., 4.3 molecules p.u.c[19]), the slight preference for *cis*-OMC over *trans*-OMC is retained, with the difference among the lowest-energy configurations amounting to 10 kJ mol^{-1} (adsorption energies are always reported per molecule, not per unit cell). The adsorption energies are about 30 kJ mol^{-1} less negative than those computed for the 1 OMC p.u.c. case, and the relative magnitude of dispersion interactions is only modestly increased. Since the symmetry had to be removed in order to distribute the cations in the NaX model over partially occupied equivalent crystallographic sites, different cages in the unit cell differ in the local arrangement of the cations. As a consequence, some of the adsorbed molecules will be located in a "non-optimal" local environment, resulting in a decrease of the total interaction strength in comparison to the 1 OMC p.u.c. case. This effect could be counterbalanced, or even outweighed, by attractive guest$-$guest interactions. The magnitude of such guest$-$guest interactions was estimated on the basis of single-point calculations for the optimized arrangement of the 4 OMC molecules, removing the NaX framework. The resulting contribution of guest$-$guest interactions is on the order of 20 to 30 kJ mol^{-1} (per

molecule), corresponding to less than 10% of the adsorption energy. Hence, it can be inferred that the OMC molecules are adsorbed largely independently from each other and that attractive interactions between them play only a secondary role. Since the energy difference between *trans*- and *cis*-OMC adsorbed in the zeolite is small, the next section will present simulated IR spectra obtained for the DFT-optimized structures. The analysis and comparison to experimental data can deliver information about the dominant isomer present in our samples.

3.3. Comparison between Computed and Experimental IR Spectra. Figure 5 compares the DFT-computed IR spectra of *trans*- and *cis*-OMC in the gas phase to the experimentally measured spectrum of the OMC in CCl$_4$ in the frequency range from 1800 to 1200 cm^{-1}. For some bands of particular relevance for the discussion, an assignment to molecular vibrational modes is made. In the frequency range of 1750 to 1600 cm^{-1}, the experimental spectrum shows three bands of significant intensity, which can be assigned to C=O stretching (1713 cm^{-1}), C=C stretching (1637 cm^{-1}), and the highest-frequency aromatic ring vibration (1605 cm^{-1}). Without the application of any scaling factor, the DFT calculations reproduce these values very well: the frequencies of the ν(C=O) vibration and the ring vibration are almost identical for *trans*-OMC/*cis*-OMC, amounting to 1707/1706 and 1605/1605 cm^{-1}. A more remarkable difference is observed for the ν(C=C) vibration, where the DFT value for *trans*-OMC of 1633 cm^{-1} agrees much better with experiment than that of *cis*-OMC (1620 cm^{-1}). As a consequence, the bands corresponding to ν(C=C) and aromatic ring vibrations are better separated in the computed spectrum of *trans*-OMC. Bands corresponding to other aromatic ring vibrations at about 1570, 1500, and 1420 cm^{-1}
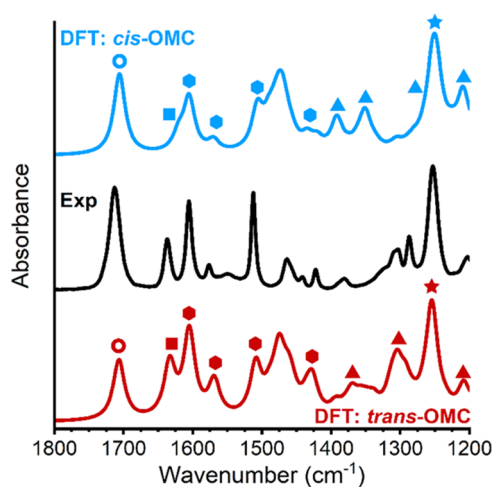
Figure 5. DFT-calculated IR spectra of the OMC isomers in the gas phase (blue/red) and experimental spectrum of the OMC in CCl_4 (black). Spectra are normalized to have the same maximal intensity and offset for clarity. In the calculated spectra, bands of particular interest are indicated by symbols: open circles: $\nu(C=O)$ vibrations, squares: $\nu(C=C)$ vibrations, hexagons: aromatic ring vibrations, triangles: rocking and scissoring vibrations of H atoms at the $C=C$ double bond, and stars: $\nu(C_{phen}-O_{meth})$ vibrations.

are present in the calculated spectrum of *trans*-OMC, although the experimental intensity ratios are not reproduced. The third of these vibrations makes almost no visible contribution to the spectrum of *cis*-OMC. Rocking and scissoring vibrations of the $C=C-H$ groups fall in the frequency range between 1400 and 1200 cm^{-1}. Two distinct bands arising from such vibrations at about 1390 and 1350 cm^{-1} in the calculated spectrum of *cis*-OMC are not observed in the experimental spectrum. The high-intensity band at about 1250 cm^{-1}, equally prominent in the DFT-computed spectra of both isomers, corresponds to a C−O stretching mode involving the O_{meth} atom (methoxy group) and the attached carbon atom of the phenyl ring. Altogether, the agreement with experiment is significantly better for the DFT-calculated spectrum of *trans*-OMC, corroborating that free OMC is present in the *trans*-form.[47]

The DFT-computed spectra for the lowest-energy adsorption configurations of *trans*- and *cis*-OMC in NaX (1 molecule p.u.c.) are compared to the experimental spectrum of NaX/OMC outgassed at 200 °C (i.e., the highest temperature before the OMC filter starts to decompose) in Figure 6a. All three spectra exhibit a red shift of the $\nu(C=O)$ vibration but with a different magnitude. Indeed, for NaX/*trans*-OMC, the calculated frequency of 1646 cm^{-1} falls fairly close to the experimentally observed band (1637 cm^{-1}). Conversely, a much larger red shift to 1570 cm^{-1} is obtained for the NaX/*cis*-OMC case, bringing about a qualitative change in the order of the three prominent maxima, i.e., $\nu(C=O)$, $\nu(C=C)$, aromatic ring, in this frequency range. Altogether, the band positions and intensity ratios fit better for NaX/*trans*-OMC than for *cis*-OMC, providing evidence that the *trans*-form remains in the adsorbed state. Moreover, if *cis*-OMC was present, then $C=C-H$ rocking and scissoring vibrations should give rise to two fairly intense bands at 1390 and 1340 cm^{-1}. For NaX/*trans*-OMC, the most intense bands arising from such vibrations fall close to 1305 cm^{-1}, better matching the (relatively weak) band at about 1295 cm^{-1} in the experimental spectrum. The $C_{phen}-O_{meth}$ stretching vibration that was observed at 1250 cm^{-1} in the spectra of free OMC is red-shifted upon adsorption. While the shift in the experimental spectrum is moderate, amounting to about 8 to 10 cm^{-1}, much more pronounced shifts are predicted in the calculations, with the band being located at 1218 cm^{-1}/1228 cm^{-1} for *trans*-OMC/*cis*-OMC adsorbed in NaX.

The analysis in the preceding paragraph focused exclusively on the lowest-energy configurations of *trans*- and *cis*-OMC in NaX. The most significant modes were also analyzed for the remaining 1 p.u.c. configurations. Typically, variations among different configurations of the same isomers are relatively small, remaining within ±10 cm^{-1}. Notable exceptions occur for some stretching vibrations of *trans*-OMC in NaX: for the $\nu(C=O)$ vibration, computed frequencies vary between 1646 and 1695 cm^{-1}. Frequencies between 1598 and 1636 cm^{-1} are predicted for the $\nu(C=C)$ vibration, and the frequency of the $\nu(C_{phen}-O_{meth})$ vibration also varies widely, from 1207 to 1263 cm^{-1}. These observations point to a considerable dependence
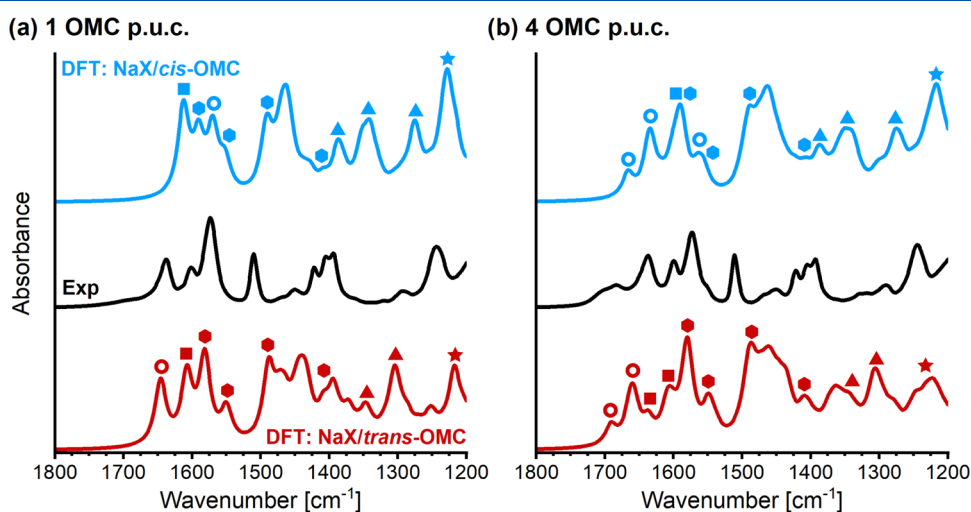

Figure 6. (a) DFT-calculated IR spectra of NaX/OMC of lowest-energy adsorption configurations at a loading of 1 OMC/p.u.c. together with the experimental spectrum of a NaX/OMC sample outgassed at 200 °C. (b) DFT-calculated spectra obtained for a loading of 4 OMC/p.u.c. together with the experimental spectrum of a sample outgassed at 150 °C. See the caption of Figure 5 for the meaning of the symbols.

of the band position on the local environment of the adsorbed molecule.

This impact of the local environment on the vibrations of adsorbed OMC molecules is also apparent when looking at the DFT-computed spectra for the lowest-energy 4 p.u.c. adsorption configurations. They are visualized in Figure 6b, together with the experimental spectrum measured for a NaX/OMC sample outgassed at 150 °C. We selected this spectrum since it is representative of a higher coverage condition with respect to the spectrum of the sample outgassed at 200 °C (reported in Figure 6a) without showing significant traces of adsorbed water. In the calculated spectra, the most prominent changes when moving from low loadings to high loadings occur in the frequency range from 1700 to 1500 cm^{-1}. In particular, there are now several signals corresponding to $\nu(C=O)$ vibrations, which can be attributed to the presence of OMC molecules in different environments. For NaX/*trans*-OMC, two distinct bands at about 1690 and 1660 cm^{-1} are visible, and the band arising from $\nu(C=C)$ vibrations also splits (1637 and 1606 cm^{-1}). In the case of NaX/*cis*-OMC, there are three discernible signals from $\nu(C=O)$ vibrations, with one of them being heavily red-shifted to 1565 cm^{-1}. Bands corresponding to $\nu(C=C)$ vibrations and aromatic ring vibrations result in one broadened peak at about 1590 cm^{-1} for NaX/*cis*-OMC. In contrast, they remain well separated for the *trans* isomer, better matching the experimental spectrum. In the lower-frequency part of the spectrum, some of the differences between the two isomers that were very visible for low loadings become less evident in the spectra computed for higher loadings. Generally, the peaks are broader due to contributions from several molecules in different environments.

In order to gain further insights into the local (non-dispersive) contributions to host−guest interactions, the computed spectra can be analyzed in combination with the DFT-optimized structures. Most emphasis in this analysis, which considered not only the lowest-energy configurations included in Figure 6 but also several additional ones from Table 1, was placed on the $\nu(C=O)$ vibrations. Interestingly, a plot of the computed frequencies against $d(Na\cdots O_{carb})$ reveals no direct correlation (Figure 7a). This shows that the elongation of the C=O double bond upon adsorption, which is essentially linearly correlated with the stretching frequency, is not a simple function of the distance to the nearest cation but that additional factors contribute to it. On a qualitative level, three scenarios can be distinguished: (1) if there are no cations within 3 Å of the O$_{carb}$ atom, the elongation is negligible, and the frequency remains close to that of free OMC (usually above 1670 cm^{-1}); (2) if there is a single cation in the vicinity, typically at distances between 2.2 and 2.4 Å, the C=O double bond is elongated, with bond distances in the range of 1.235 Å to 1.250 Å, and frequencies mostly falling in an interval from 1610 to 1670 cm^{-1}; and (3) a "dual-site" interaction with two Na cations results in even stronger elongations (>1.25 Å) and more pronounced red shifts in the stretching frequency, typically from 1560 to 1570 cm^{-1}. Such dual-site interactions, which have been reported, for example, for carbon monoxide in Na-containing zeolites,[48−50] are predicted only for *cis*-OMC. This peculiarity is related to the geometry of the *cis* isomer, whose carbonyl group points away from the bulkier parts of the molecule, reducing steric repulsion. While only one cation in the vicinity of the carbonyl group is shown in Figure 4, it is worth noting that a secondary
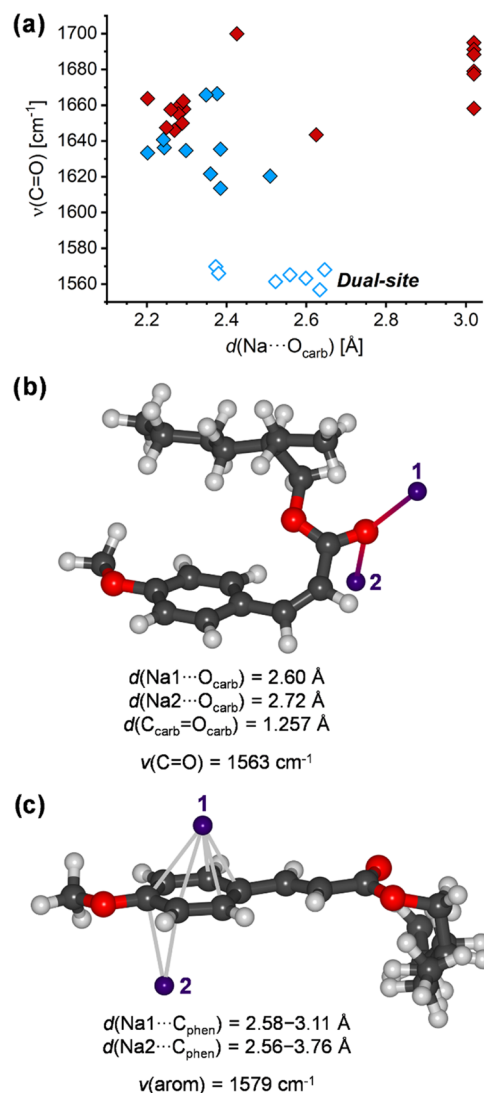

Figure 7. (a) Calculated frequencies of $\nu(C=O)$ stretching mode plotted against distance $d(Na\cdots O_{carb})$. Data points for *cis*-OMC and *trans*-OMC are represented by blue and red diamonds, respectively. For dual-site coordination of *cis*-OMC (open symbols), points are shown at the lower of the two Na$\cdots$O$_{carb}$ distances. If no contacts below 3 Å are present, the frequency is plotted at an arbitrary distance of 3.02 Å. (b) Representative example of a dual-site coordination of the carbonyl group of *cis*-OMC to two Na cations. (c) Representative example of an interaction of the *trans*-OMC phenyl ring with two Na cations, with Na$\cdots$C$_{phen}$ distances below 3 Å shown as thin gray lines. Other cations and the zeolite framework are omitted from the visualization in both panels.

contact with another cation with a distance of 3.02 Å is present. A more typical dual-site scenario is visualized in Figure 7b. With regard to the C=C double bond, the variation of the calculated frequencies of the $\nu(C=C)$ stretching mode points to considerable sensitivity to the local environment; however, no apparent correlations to other interatomic distances could be deduced. The more pronounced red shift of the highest aromatic ring vibration for NaX/*trans*-OMC can be explained with the better accessibility of the phenyl ring of this isomer, which is conducive to stronger cation−π interactions. A representative example of an adsorption configuration with two Na cations in the direct vicinity of the phenyl ring is shown in Figure 7c. In that particular case, the red shift with respect to

free *trans*-OMC exceeds 25 cm^{-1}. Finally, the frequency of the $\nu(C_{phen}-O_{meth})$ vibration is also affected by the presence of Na cations in the vicinity. Again, the red shift is not directly correlated with the distance, with frequencies between 1240 and 1215 cm^{-1} occurring in configurations where $d(Na\cdots O_{meth})$ falls between 2.28 and 2.47 Å. Even more pronounced red shifts to about 1205 cm^{-1} are observed in cases of dual-site interactions of O_{meth} with two Na cations. In view of the observation of different types of localized interactions between adsorbed OMC and Na cations, it is worth noting that the cation displacements in the DFT-optimized structures of OMC-loaded NaX with respect to guest-free NaX are very small, remaining below 0.01 Å.

Altogether, the body of evidence obtained from the combination of IR spectroscopy and DFT shows that OMC adsorbed in NaX is dominantly present in the *trans*-form. As the calculations predict that *cis*-OMC should be energetically slightly favored in the adsorbed state, it is useful to consider possible reasons why there is no evidence for *cis*-OMC in real NaX samples. First of all, the computational approach, based on Monte Carlo insertions of the two isomers prior to the DFT optimizations, does not permit any conclusions as to whether conversion between them could occur in the pores of NaX. It can be hypothesized that the confinement exerted by the zeolite renders the transition state inaccessible, thus precluding an isomerization of adsorbed *trans*-OMC to the *cis* form despite the slight thermodynamic preference. This kind of "transition state selectivity" is not an uncommon phenomenon in zeolites.[51] In order to further evaluate the possible limitations of a *trans*-*cis* conversion in the zeolite pores, the transition pathway was predicted by using constrained optimizations, varying the H−C≡C−H dihedral angle. These calculations used a complete active space self-consistent field (CASSCF) formalism, employing the ORCA code[52] with def2-TZVP basis sets.[53] Further details are supplied in section S3 of the Supporting Information. Figure S3 shows the two end points, *trans*- and *cis*-OMC, and the five selected intermediate states. It is clearly visible that the transition from the more elongated *trans* isomer to the more compact *cis* isomer corresponds to a "folding" of the molecule. As illustrated in Figure 3, *trans*-OMC spans two supercages in the lowest-energy configuration, with the central part of the molecule being located at the 12MR window. In other configurations, at least the terminal methoxy group protrudes through one of the windows. Consequently, the "folding" required for the isomerization would almost inevitably result in a collision of one part of the molecule with some atoms of the framework. Hence, it is reasonable to conclude that the transition to *cis*-OMC is much less likely to occur when adsorbed in the zeolite pores than in the liquid phase.

Another possible pathway to the formation of *cis*-OMC/NaX would be conversion prior to adsorption. While *cis*-OMC should be preferentially adsorbed, its bulky nature might impede diffusion into the structure. Indeed, preliminary force field molecular dynamics simulations (NVT ensemble, $T = 100$ °C, COMPASS III force field, see section S4 of the Supporting Information for more details) of OMC in an all-silica model of FAU delivered an appreciable mobility of *trans*-OMC on the time scale of the simulations. The self-diffusion coefficient (averaged over 5 independent trajectories) amounts to 342 ± 84 × 10^{-8} cm^2 s^{-1}. Self-diffusion coefficients on the same order of magnitude were predicted for triclosan in all-silica FAU at room temperature.[54] In contrast, *cis*-OMC always remained in

the same supercage over the course of the 50 ns MD simulation, both in all-silica FAU and in NaX. For the case of *trans*-OMC in NaX, a movement of the molecule from one 12MR to an adjacent one during the simulation was observed in one of the five trajectories, whereas only oscillations about the initial location occurred in the other four trajectories. Even though this result does not permit a reasonably accurate quantitative determination of the self-diffusion coefficient, the whole body of results obtained for all-silica FAU and NaX clearly points to a significantly higher diffusivity of *trans*-OMC in comparison to *cis*-OMC.

4. CONCLUSIONS

From our combined experimental/computational approach, it has been possible to unravel the nature and the host−guest interactions of the UV filter molecules adsorbed in NaX zeolites. Due to the complexity of the system, the understanding of the structural features of the hybrid would have been impossible using conventional diffractometric techniques previously exploited for systems with lower symmetry.[26]

Infrared spectra showed in the as-synthesized sample the presence of a small fraction of loosely bound molecules located on the external zeolite surface. Moreover, progressive lowering of the OMC loading by outgassing highlighted that in this hybrid material, the molecules of the OMC are adsorbed in different environments, giving rise to complex IR spectra that could not be easily interpreted without the support of thorough computational modeling.

The DFT calculations predicted that *cis*-OMC should be energetically slightly favored in the adsorbed state, but a systematic comparison with the experimental spectroscopic results allowed us to conclude that the OMC is mainly present in the *trans*-form. Indeed, the experimentally observed $\nu(C= O)$ red shift, due to the interaction with the Na cations, is better described by the *trans*-OMC model. Moreover, the $\nu(C=C)$ and the highest aromatic ring vibration are well separated in the experiment, and the more pronounced red shift of the highest-frequency aromatic ring vibration predicted for *trans*-OMC better corresponds to the experimental findings.

A possible explanation for the absence of adsorbed *cis*-OMC in the samples could be related to the bulky nature of this isomer, which might hinder its diffusion into the zeolite structure. Moreover, geometric considerations corroborated by CASSCF calculations of the transition pathway indicate that the confinement exerted by the zeolite renders the *trans*-*cis* transition state inaccessible, thus precluding an isomerization of adsorbed *trans*-OMC to the *cis* form, despite the slight thermodynamic preference.

The results of this joint experimental/computational study show that the Na ions in the zeolite framework are able to provide strong host−guest interactions, which hinder the release of the OMC in the environment. On the other hand, the relative contribution of dispersion interactions typically amounts to about 50% of the total adsorption energy. Moreover, the encapsulation minimizes the interactions between filter molecules, which can lead to photochemical instability,[55] as well as potentially suppress unwanted isomerization reactions, which would reduce the UV filtering capacity.[56,57] These evidence suggest that cationic zeolites are promising materials for the production of hybrid UV filters and that other framework topologies should be explored, trying

to maximize the weight percentage of organic filters in the system.

ASSOCIATED CONTENT

Supporting Information

The Supporting Information is available free of charge at https://pubs.acs.org/doi/10.1021/acs.jpcc.3c05854.

> Further information on the cation distribution in the NaX structure model used in the DFT calculations (section S1), a table of force field and DFT energies (section S2), details and results of CASSCF calculations (section S3), and details and results of MD simulations (section S4) (PDF)
>
> Other supplementary files comprise DFT-optimized configurations (in PDB format) and MOLDEN.mol files containing frequencies and intensities of DFT-calculated vibrational modes of OMC (ZIP)

AUTHOR INFORMATION

Corresponding Author

Lorenzo Mino — *Department of Chemistry and NIS Centre, University of Torino, I-10125 Torino, Italy;* ● orcid.org/0000-0002-9882-8361; Email: lorenzo.mino@unito.it

Authors

Michael Fischer — *Crystallography & Geomaterials Research, Faculty of Geosciences, and Bremen Center for Computational Materials Science, and MAPEX Center for Materials and Processes, University of Bremen, D-28359 Bremen, Germany;* ● orcid.org/0000-0001-5133-1537

Riccardo Fantini — *Department of Chemical and Geological Sciences, University of Modena and Reggio Emilia, I-41125 Modena, Italy*

Rossella Arletti — *Department of Chemical and Geological Sciences, University of Modena and Reggio Emilia, I-41125 Modena, Italy;* ● orcid.org/0000-0001-9878-8657

Jakob Brauer — *Crystallography & Geomaterials Research, Faculty of Geosciences, and Bremen Center for Computational Materials Science, and MAPEX Center for Materials and Processes, University of Bremen, D-28359 Bremen, Germany*

Complete contact information is available at:
https://pubs.acs.org/10.1021/acs.jpcc.3c05854

Notes

The authors declare no competing financial interest.

REFERENCES

(1) World Health Organization. *Environmental Health Criteria 160: Ultraviolet Radiation*; WHO: Geneva, 1994.

(2) Sequeira, V. B.; Rybchyn, M. S.; Tongkao-on, W.; Tongkao-On, W.; Gordon-Thomson, C.; Malloy, P. J.; Nemere, I.; Norman, A. W.; Reeve, V. E.; Halliday, G. M.; Feldman, D. The Role of the Vitamin D Receptor and ERp57 in Photoprotection by 1α,25-Dihydroxyvitamin D3. *Mol. Endocrinol.* **2012**, *26* (4), 574−582.

(3) Chen, P.-J.; Nakano, T.; Lai, C.-Y.; Chang, K.-C.; Chen, C.-L.; Goto, S. Daily Full Spectrum Light Exposure Prevents Food Allergy-like Allergic Diarrhea by Modulating Vitamin D3 and Microbiota Composition. *NPJ. Biofilms Microbiomes* **2021**, *7* (1), 41.

(4) Osterwalder, U.; Sohn, M.; Herzog, B. Global State of Sunscreens. *Photodermatol. Photoimmunol. Photomed.* **2014**, *30* (2−3), 62−80.

(5) Gies, P.; van Deventer, E.; Green, A. C.; Sinclair, C.; Tinker, R. Review of the Global Solar UV Index 2015 Workshop Report. *Health Phys.* **2018**, *114* (1), 84−90.

(6) Apalla, Z.; Nashan, D.; Weller, R. B.; Castellsagué, X. Skin Cancer: Epidemiology, Disease Burden, Pathophysiology, Diagnosis, and Therapeutic Approaches. *Dermatol. Ther.* **2017**, *7* (Suppl 1), 5−19.

(7) Information and Resources about for Cancer: Breast, Colon, Lung, Prostate, Skin | American Cancer Society. https://www.cancer.org/ (accessed Aug 21, 2023).

(8) Forsea, A.-M. Melanoma Epidemiology and Early Detection in Europe: Diversity and Disparities. *Dermatol. Pract. Concept.* **2020**, *10* (3), e2020033.

(9) Martens, M. C.; Seebode, C.; Lehmann, J.; Emmert, S. Photocarcinogenesis and Skin Cancer Prevention Strategies: An Update. *Anticancer Res.* **2018**, *38* (2), 1153−1158.

(10) Langford, K. H.; Reid, M. J.; Fjeld, E.; Øxnevad, S.; Thomas, K. V. Environmental Occurrence and Risk of Organic UV Filters and Stabilizers in Multiple Matrices in Norway. *Environ. Int.* **2015**, *80*, 1−7.

(11) Damiani, E.; Puglia, C. Nanocarriers and Microcarriers for Enhancing the UV Protection of Sunscreens: An Overview. *J. Pharm. Sci.* **2019**, *108* (12), 3769−3780.

(12) Afonso, S.; Horita, K.; Sousa e Silva, J. P.; Almeida, I. F.; Amaral, M. H.; Lobão, P. A.; Costa, P. C.; Miranda, M. S.; Esteves da Silva, J. C. G.; Sousa Lobo, J. M. Photodegradation of Avobenzone: Stabilization Effect of Antioxidants. *J. Photochem. Photobiol., B* **2014**, *140*, 36−40.

(13) Cozzi, A. C.; Perugini, P.; Gourion-Arsiquaud, S. Comparative Behavior between Sunscreens Based on Free or Encapsulated UV Filters in Term of Skin Penetration, Retention and Photo-Stability. *Eur. J. Pharm. Sci.* **2018**, *121*, 309−318.

(14) Vione, D.; Calza, P.; Galli, F.; Fabbri, D.; Santoro, V.; Medana, C. The Role of Direct Photolysis and Indirect Photochemistry in the Environmental Fate of Ethylhexyl Methoxy Cinnamate (EHMC) in Surface Waters. *Sci. Total Environ.* **2015**, *537*, 58−68.

(15) Cadena-Aizaga, M. I.; Montesdeoca-Esponda, S.; Sosa-Ferrera, Z.; Santana-Rodríguez, J. J. Occurrence and Environmental Hazard of Organic UV Filters in Seawater and Wastewater from Gran Canaria Island (Canary Islands, Spain). *Environ. Pollut.* **2022**, *300*, No. 118843.

(16) Zenker, A.; Schmutz, H.; Fent, K. Simultaneous Trace Determination of Nine Organic UV-Absorbing Compounds (UV Filters) in Environmental Samples. *J. Chromatogr. A* **2008**, *1202* (1), 64−74.

(17) Bachelot, M.; Li, Z.; Munaron, D.; Le Gall, P.; Casellas, C.; Fenet, H.; Gomez, E. Organic UV Filter Concentrations in Marine Mussels from French Coastal Regions. *Sci. Total Environ.* **2012**, *420*, 273−279.

(18) Corinaldesi, C.; Damiani, E.; Marcellini, F.; Falugi, C.; Tiano, L.; Brugè, F.; Danovaro, R. Sunscreen Products Impair the Early Developmental Stages of the Sea Urchin Paracentrotus Lividus. *Sci. Rep.* **2017**, *7* (1), 7815.

(19) Fantini, R.; Vezzalini, G.; Zambon, A.; Ferrari, E.; Di Renzo, F.; Fabbiani, M.; Arletti, R. Boosting Sunscreen Stability: New Hybrid Materials from UV Filters Encapsulation. *Microporous Mesoporous Mater.* **2021**, *328*, 111478.

(20) Baerlocher, C.; McCusker, L. B.; Olson, D.; Meier, W. M. Atlas of Zeolite Framework Types. In *Published on Behalf of the Structure Commission of the International Zeolite Association*, 6th Rev ed.; Elsevier: Amsterdam Boston, 2007.

(21) Calzaferri, G.; Brühwiler, D.; Megelski, S.; Pfenniger, M.; Pauchard, M.; Hennessy, B.; Maas, H.; Devaux, A.; Graf, U. Playing with Dye Molecules at the Inner and Outer Surface of Zeolite L. *Solid State Sci.* **2000**, *2* (4), 421−447.

(22) Scelta, D.; Ceppatelli, M.; Santoro, M.; Bini, R.; Gorelli, F. A.; Perucchi, A.; Mezouar, M.; van der Lee, A.; Haines, J. High Pressure Polymerization in a Confined Space: Conjugated Chain/Zeolite Nanocomposites. *Chem. Mater.* **2014**, *26* (7), 2249−2255.

(23) Calzaferri, G. Nanochannels: Hosts for the Supramolecular Organization of Molecules and Complexes. *Langmuir* **2012**, *28* (15), 6216−6231.

(24) Fabbiani, M.; Confalonieri, G.; Morandi, S.; Arletti, R.; Quartieri, S.; Santoro, M.; Di Renzo, F.; Haines, J.; Fantini, R.; Tabacchi, G.; et al. Steering Polymer Growth by Molding Nano-channels: 1,5-Hexadiene Polymerization in High Silica Mordenite. *Microporous Mesoporous Mater.* **2021**, *311*, 110728.

(25) Gigli, L.; Arletti, R.; Vitillo, J. G.; Alberto, G.; Martra, G.; Devaux, A.; Vezzalini, G. Thionine Dye Confined in Zeolite L: Synthesis Location and Optical Properties. *J. Phys. Chem. C* **2015**, *119* (28), 16156−16165.

(26) Confalonieri, G.; Fantini, R.; Allasia, N.; Vezzalini, G.; Fitch, A. N.; Mino, L.; Arletti, R. Structural Evidence of Sunscreen Enhanced Stability in UV Filter-Zeolite Hybrids. *Microporous Mesoporous Mater.* **2022**, *344*, 112212.

(27) Pavan, C.; Santalucia, R.; Escolano-Casado, G.; Ugliengo, P.; Mino, L.; Turci, F. Physico-Chemical Approaches to Investigate Surface Hydroxyls as Determinants of Molecular Initiating Events in Oxide Particle Toxicity. *Int. J. Mol. Sci.* **2023**, *24* (14), 11482.

(28) Polisi, M.; Grand, J.; Arletti, R.; Barrier, N.; Komaty, S.; Zaarour, M.; Mintova, S.; Vezzalini, G. CO₂ Adsorption/Desorption in FAU Zeolite Nanocrystals: In Situ Synchrotron X-Ray Powder Diffraction and in Situ Fourier Transform Infrared Spectroscopic Study. *J. Phys. Chem. C* **2019**, *123* (4), 2361−2369.

(29) Fois, E.; Oriani, M.; Tabacchi, G. A Post-HF Approach to the Sunscreen Octyl Methoxycinnamate. *J. Chem. Phys.* **2021**, *154* (14), 144304.

(30) Akkermans, R. L. C.; Spenley, N. A.; Robertson, S. H. COMPASS III: Automated Fitting Workflows and Extension to Ionic Liquids. *Mol. Simul.* **2021**, *47* (7), 540−551.

(31) VandeVondele, J.; Krack, M.; Mohamed, F.; Parrinello, M.; Chassaing, T.; Hutter, J. Quickstep: Fast and Accurate Density Functional Calculations Using a Mixed Gaussian and Plane Waves Approach. *Comput. Phys. Commun.* **2005**, *167* (2), 103−128.

(32) Kühne, T. D.; Iannuzzi, M.; Del Ben, M.; Rybkin, V. V.; Seewald, P.; Stein, F.; Laino, T.; Khaliullin, R. Z.; Schütt, O.; Schiffmann, F.; et al. CP2K: An Electronic Structure and Molecular Dynamics Software Package - Quickstep: Efficient and Accurate Electronic Structure Calculations. *J. Chem. Phys.* **2020**, *152* (19), 194103.

(33) Hamada, I. Van Der Waals Density Functional Made Accurate. *Phys. Rev. B* **2014**, *89* (12), 121103.

(34) VandeVondele, J.; Hutter, J. Gaussian Basis Sets for Accurate Calculations on Molecular Systems in Gas and Condensed Phases. *J. Chem. Phys.* **2007**, *127* (11), 114105.

(35) Krack, M. Pseudopotentials for H to Kr Optimized for Gradient-Corrected Exchange-Correlation Functionals. *Theor. Chem. Acc.* **2005**, *114* (1), 145−152.

(36) Fischer, M. Adsorption of Carbamazepine in All-Silica Zeolites Studied with Density Functional Theory Calculations. *ChemPhysChem* **2023**, *24* (9), e202300022.

(37) Schaftenaar, G.; Noordik, J. H. Molden: A Pre- and Post-Processing Program for Molecular and Electronic Structures. *J. Comput. Aided Mol. Des.* **2000**, *14* (2), 123−134.

(38) Perdew, J. P.; Burke, K.; Ernzerhof, M. Generalized Gradient Approximation Made Simple. *Phys. Rev. Lett.* **1996**, *77* (18), 3865−3868.

(39) Grimme, S.; Antony, J.; Ehrlich, S.; Krieg, H. A Consistent and Accurate Ab Initio Parametrization of Density Functional Dispersion Correction (DFT-D) for the 94 Elements H-Pu. *J. Chem. Phys.* **2010**, *132* (15), 154104.

(40) Mino, L.; Negri, C.; Santalucia, R.; Cerrato, G.; Spoto, G.; Martra, G. Morphology, Surface Structure and Water Adsorption Properties of TiO₂ Nanoparticles: A Comparison of Different Commercial Samples. *Molecules* **2020**, *25* (20), 4605.

(41) Mino, L.; Morales-García, Á.; Bromley, S. T.; Illas, F. Understanding the Nature and Location of Hydroxyl Groups on Hydrated Titania Nanoparticles. *Nanoscale* **2021**, *13* (13), 6577−6585.

(42) Montanari, T.; Finocchio, E.; Busca, G. Infrared Spectroscopy of Heterogeneous Catalysts: Acidity and Accessibility of Acid Sites of Faujasite-Type Solid Acids. *J. Phys. Chem. C* **2011**, *115* (4), 937−943.

(43) Lønstad Bleken, B.-T.; Mino, L.; Giordanino, F.; Beato, P.; Svelle, S.; Lillerud, K. P.; Bordiga, S. Probing the Surface of Nanosheet H-ZSM-5 with FTIR Spectroscopy. *Phys. Chem. Chem. Phys.* **2013**, *15* (32), 13363−13370.

(44) Datka, J.; Boczar, M.; Gil, B. Heterogeneity of Hydroxyl Groups in Zeolites Studied by IR Spectroscopy. *Colloids Surf. Physicochem. Eng. Asp.* **1995**, *105* (1), 1−18.

(45) Wang, H.; Grant, D. J.; Burns, P. C.; Na, C. Infrared Signature of the Cation-π Interaction between Calcite and Aromatic Hydro-carbons. *Langmuir ACS J. Surf. Colloids* **2015**, *31* (21), 5820−5826.

(46) Thomas, K. J.; Sunoj, R. B.; Chandrasekhar, J.; Ramamurthy, V. Cation-π-Interaction Promoted Aggregation of Aromatic Molecules and Energy Transfer within Y Zeolites. *Langmuir* **2000**, *16* (11), 4912−4921.

(47) Sayre, R. M.; Dowdy, J. C.; Gerwig, A. J.; Shlelds, W. J.; Lioyd, R. V. Unexpected Photolysis of the Sunscreen Octinoxate in the Presence of the Sunscreen Avobenzone. *Photochem. Photobiol.* **2005**, *81* (2), 452−456.

(48) Nachtigall, P.; Rodríguez Delgado, M.; Frolich, K.; Bulánek, R.; Turnes Palomino, G.; López Bauçà, C.; Otero Areán, C. Periodic Density Functional and FTIR Spectroscopic Studies on CO Adsorption on the Zeolite Na-FER. *Microporous Mesoporous Mater.* **2007**, *106* (1−3), 162−173.

(49) Fischer, M.; Delgado, M. R.; Areán, C. O.; Duran, C. O. CO Adsorption Complexes in Zeolites: How Does the Inclusion of Dispersion Interactions Affect Predictions Made from DFT Calculations? The Case of Na-CHA. *Theor. Chem. Acc.* **2015**, *134* (7), 91.

(50) Otero Areán, C.; Delgado, M. R.; Bauçà, C. L.; Vrbka, L.; Nachtigall, P. Carbon Monoxide Adsorption on Low-Silica Zeolites—from Single to Dual and to Multiple Cation Sites. *Phys. Chem. Chem. Phys.* **2007**, *9* (33), 4657−4661.

(51) Wright, P. A. *Microporous Framework Solids*; Royal Society of Chemistry, 2007.

(52) Neese, F.; Wennmohs, F.; Becker, U.; Riplinger, C. The ORCA Quantum Chemistry Program Package. *J. Chem. Phys.* **2020**, *152* (22), 224108.

(53) Weigend, F.; Ahlrichs, R. Balanced Basis Sets of Split Valence, Triple Zeta Valence and Quadruple Zeta Valence Quality for H to Rn: Design and Assessment of Accuracy. *Phys. Chem. Chem. Phys.* **2005**, *7* (18), 3297−3305.

(54) Fischer, M. Density Functional Theory Study of Hydrophobic Zeolites for the Removal of Triclosan from Aqueous Solution. *Environ. Sci. Adv.* **2023**, *2* (8), 1082−1098.

(55) Hanson, K. M.; Narayanan, S.; Nichols, V. M.; Bardeen, C. J. Photochemical Degradation of the UV Filter Octyl Methoxycinnamate in Solution and in Aggregates. *Photochem. Photobiol. Sci.* **2015**, *14* (9), 1607−1616.

(56) Dondi, D.; Albini, A.; Serpone, N. Interactions between Different Solar UVB/UVA Filters Contained in Commercial Suncreams and Consequent Loss of UV Protection. *Photochem. Photobiol. Sci.* **2006**, *5* (9), 835−843.

(57) Hopkins, Z. R.; Snowberger, S.; Blaney, L. Ozonation of the Oxybenzone, Octinoxate, and Octocrylene UV-Filters: Reaction Kinetics, Absorbance Characteristics, and Transformation Products. *J. Hazard. Mater.* **2017**, *338*, 23−32.